



ELSEVIER

Available online at www.sciencedirect.com

SCIENCE @ DIRECT®

Journal of Sound and Vibration 282 (2005) 313–339

JOURNAL OF
SOUND AND
VIBRATION

www.elsevier.com/locate/jsvi

Acoustic radiation from out-of-plane modes of an annular disk using thin and thick plate theories

Hyeongill Lee, Rajendra Singh*

Acoustics and Dynamics Laboratory, Department of Mechanical Engineering, The Center for Automotive Research, The Ohio State University, Columbus, OH 43210, USA

Received 19 August 2002; accepted 20 February 2004

Abstract

Out-of-plane (flexural) vibration is a major source of sound radiation from many mechanical or structural components having annular or circular disk shape. The typical thickness of practical components is often beyond the thin plate theory limit and it may have considerable effect on sound radiation. But, traditionally, thin annular disk models have been employed for such structures neglecting the thickness effect. In this article, structural eigensolutions for the out-of-plane modes and sound radiation from the modal vibration of a thick annular disk with free–free boundaries have been calculated using both thick and thin plate theories. A new analytical formulation is proposed for the sound radiation problem. In addition, the same problem has been solved by a semi-analytical procedure in which the disk surface velocity is numerically defined by a finite-element model and sound radiation is then analytically obtained using a modified circular radiator model. Also, the effects of radii and thickness ratios on the structural and acoustic radiation characteristics are investigated using the analytical procedure. Finally, the effect of boundary conditions is briefly examined.

© 2004 Elsevier Ltd. All rights reserved.

1. Introduction

Acoustic radiation from thick plates or disks has not been adequately examined though there is a substantial body of literature on the structural dynamics of thin and thick plates [1–9]. Limited

*Corresponding author. Tel.: +1-614-292-9044; fax: +1-614-292-3163.

E-mail address: singh.3@osu.edu (R. Singh).

Nomenclature

a	outer radius of annular disk (mm)	$[T_{\text{THIN}}]$	characteristic matrix for the thin plate theory
b	inner radius of annular disk (mm)	V	acoustic control volume
B	Hankel transform	w	transverse displacement in the disk (m)
c_0	speed of sound in the acoustic medium (m/s)	W	spatial dependent transverse displacement in the disk (m)
D_b	flexural rigidity of disk (Nm)	β	radii ratio of the annular disk
E	Young's modulus of disk (N/m ²)	η	angle between the surface normal vector and the vector from source position to receiver position (rad)
$f(t)$	dynamic force on disk (N)	$\Delta\theta$	increment in the cone angle θ (rad)
F	amplitude of applied force (N)	λ_{mn}	dimensionless structural eigenvalue for the (m,n) th flexural mode
g	free-field Green function	ν	Poisson's ratio of disk
i	$\sqrt{-1}$	Π	acoustic power from the disk vibration (W)
k	acoustic wave number (rad/m)	Π_{mn}	acoustic power from the modal vibrations of the disk (W)
h	disk thickness (mm)	ρ_0	mass density of the acoustic medium (kg/m ³)
\bar{h}	disk thickness ratio (h/a)	ρ_d	mass density of the disk (kg/m ³)
m	number of nodal circles in the disk	σ_{mn}	sound radiation efficiency of normal modes of the disk
$M_r, M_\phi, M_{r\phi}$	bending moment in the disk (Nm)	φ	azimuthal angle of the disk (rad)
n	number of nodal diameters in the disk	$\Delta\phi$	increment in azimuthal angle ϕ (rad)
\bar{n}	surface normal vector at the given source position	\mathfrak{R}	radiation resistance of disk
p	far-field sound pressure (Pa)	Φ_{mn}	flexural mode shape of the disk
P	spatially-dependent far-field sound pressure amplitude (Pa)	Ψ_r, Ψ_ϕ	bending rotations of the disk (rad)
P_{mn}	far-field sound pressure amplitude due to the (m, n) th out-of-plane mode (Pa)	ψ_r, ψ_ϕ	spatially dependent bending rotations of the disk (rad)
R	radius of sphere at the far-field location (m)	ω	angular frequency (rad/s)
Q_r, Q_ϕ	shear forces in the disk (N)	ω_{mn}	natural frequency of the (m, n) th out-of-plane mode (kHz)
r, ϕ, z	cylindrical coordinates	ζ_{mn}	modal damping ratio of the (m, n) th out-of-plane mode (%)
R, θ, ϕ	spherical coordinates		
r_f	position vector of the excitation force $f(t)$ on the disk		
r_p	position vector of a receiver position sound pressure		
r_s	position vector of a sound source position		
S_o	surface of the sound source		
S_v	boundary surface of the acoustic control volume		
$[T_{\text{THICK}}]$	characteristic matrix for the thick plate theory	Subscripts	
		d	disk
		m, n	out-of-plane mode indices
		0	acoustic medium

		<i>Abbreviations</i>	
p	observation point in a far-field location		
r	radial direction of the disk	BEM	boundary element method
s	source (radiator)	FEM	finite element method
φ	circumferential direction of the disk		

acoustic studies have considered either flexural vibration modes or rigid body piston motions of thin disks [11–15]. In this article, new analytical and semi-analytical methods for sound radiation from a thick annular disk will be proposed. In particular, we comparatively evaluate the merits of thin vs. thick plate theories on the calculation of radiation from out-of-plane flexural modes. Vibro-acoustic experiments and large-scale finite and boundary elements codes are used to validate the analytical formulations.

Annular disk idealization can be used to analyze many real-life mechanical components such as gears, brake rotors, clutches, flywheels, railway wheels, circular saws, and electric motor. In many cases, thickness (h) is not negligible relative to other dimensions of the component, and thus one must consider the thickness effects in structural dynamic and acoustic radiation characteristics. Fig. 1 illustrates the example case that is assumed to be non-rotating and without the complicating effects of an inner hub. The disk is assumed to be of uniform h and made of an undamped, isotropic material. First, free–free boundaries at the inner and outer edges are assumed. Then, the inner edge is assumed to be ideally fixed but the outer edge is still free. Table 1 provides typical values of 3 disks. Disk I is used for all analytical, numerical, and experimental studies. Additionally, Disks II and III are used for structural modal analysis to examine plate theories.

For a complete investigation of the vibro-acoustic characteristics of a thick annular disk, it is necessary to simultaneously consider both in-plane and out-of-plane vibrations. But, the current analysis focuses only on the out-of-plane modal vibration and the resulting sound. Primary assumptions are as follows: (1) Structural and acoustic systems are linear time-invariant systems and complicating effects such as fluid loading and acoustic scattering from the disk edges are negligible. (2) Structural velocities in the normal direction (z) vary sinusoidally in the φ direction. (3) Free and far-field sound pressure at the observation point (r_p) is generated only by the structural motions of two normal surfaces and the inner or outer radial surfaces at edges does not contribute to the far-field sound. (4) Coupling between in-plane and out-of-plane modes is negligible.

Chief objectives of this article are as follows. (1) Critically examine thick and thin plate theories and investigate the effect of rotary inertia and shear deformations on the structural eigensolutions and acoustic sound radiation. (2) Develop analytical and semi-analytical solutions for sound radiation from modal vibrations. (3) Validate analytical solutions using computational and/or experimental vibro-acoustic methods. (4) Study the effects of the disk geometry and boundary conditions on sound radiation using the proposed analytical solutions. Only single-mode excitations are considered here as the multi-modal excitations and coupling issues will be considered in a future article. Table 2 summarizes various models or methods that will be employed in this study. For the analytical method, the procedure includes the analytical

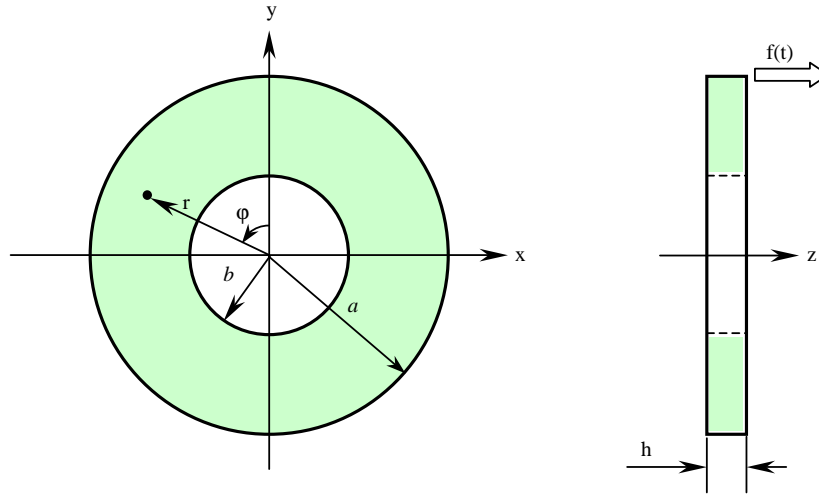


Fig. 1. A thick annular disk with free-free or fixed at $(r=b)$ - free boundaries.

Table 1
Disk examples with free-free or fixed $(r=b)$ -free boundaries

	Disk I	Disk II	Disk III
Outer radius a (mm)	151.5	139.0	151.5
Inner radius b (mm)	82.5	82.5	82.5
Radii ratio $\beta (=b/a)$	0.54	0.59	0.54
Thickness h (mm)	31.5	31.5	16.3
Thickness ratio $\bar{h}(=h/a)$	0.21	0.23	0.11
Density ρ_d (kg/m ³)	7905.9	7905.9	7905.9
Young's modulus E (GPa)	218	218	218
Poisson's ratio ν	0.305	0.305	0.305

determination of structural eigensolutions and the resulting sound field. Conversely, the finite-element method (FEM) is used for structural analysis for the semi-analytical formulation though the sound field is still computed using a modified circular disk radiator model.

2. Structural analysis based on thick and thin plate theories

2.1. Thick plate theory

According to the procedure proposed by Mindlin and Deresiewicz [7] or Mcgee et al. [8], the vibratory displacements of a thick annular disk are assumed as follows, while recognizing the

Table 2
List of models developed and methods employed for Disk I

Medium	Model or method designation	Structural dynamics formulation	Acoustic radiation formulation	Disk boundaries	Method type
Structural dynamics	A	Thick plate	—	Free–free	Analytical
	B	Thick plate - without rotary inertia effect	—	Free–free	Analytical
	C	Thin plate	—	Free–free	Analytical
	D	Finite elements	—	Free–free	Computational
	E	Experiment	—	Free–free	Experimental
	F	Thick plate	—	Fixed–free	Analytical
	G	Thick plate without rotary inertia effect	—	Fixed–free	Analytical
	H	Thin plate	—	Fixed–free	Analytical
	I	Finite elements	—	Fixed–free	Computational
Structural dynamics + acoustic radiation	J	Thick plate	Thick plate	Free–free	Analytical
	K	Thin plate	Thin plate	Free–free	Analytical
	L	Finite elements	Thick plate	Free–free	Semi-analytical
	M	Finite elements	Boundary elements	Free–free	Computational
	N	Experiment	Experiment	Free–free	Experimental
	O	Finite elements	Boundary elements	Fixed–free	Computational

effects of shear and rotating inertia.

$$u_r = z\Psi_r(r, \varphi, t), u_\varphi = z\Psi_\varphi(r, \varphi, t), w = w(r, \varphi, t). \tag{1}$$

Here, u_r , u_φ , and w are components in the radial (r), circumferential (φ), and transverse directions (z), Ψ_r and Ψ_φ are the bending rotations of normal to the mid-plane in radial and circumferential directions, respectively. Refer to nomenclature for a complete list of symbols. The equations of motion in terms of the stress resultants in polar coordinates (r, φ) are

$$\frac{\partial M_r}{\partial r} + \frac{1}{r} \frac{\partial M_\varphi}{\partial \varphi} + \frac{1}{r} (M_r - M_\varphi) - Q_r = \frac{\rho_d h^3}{12} \frac{\partial^2 \Psi_r}{\partial t^2}. \tag{2}$$

$$\frac{\partial M_{r\varphi}}{\partial r} + \frac{1}{r} \frac{\partial M_\varphi}{\partial \varphi} + \frac{2}{r} M_{r\varphi} - Q_\varphi = \frac{\rho_d h^3}{12} \frac{\partial^2 \Psi_\varphi}{\partial t^2}. \tag{3}$$

$$\frac{\partial Q_r}{\partial r} + \frac{1}{r} \frac{\partial Q_\varphi}{\partial \varphi} + \frac{1}{r} Q_r - Q_\varphi = \rho_d h \frac{\partial^2 w}{\partial t^2}, \tag{4}$$

where ρ_d is the mass density of the annular disk. The stress resultants in terms of moments M_r , M_φ , and $M_{r\varphi}$, along with shear forces Q_r and Q_φ can be related to the transverse displacements

and bending rotations as

$$M_r = D_b \left\{ \frac{\partial \Psi_r}{\partial r} + \frac{\nu}{r} \left(\Psi_r + \frac{\partial \Psi_\varphi}{\partial \varphi} \right) \right\}, \quad M_\varphi = D_b \left\{ \frac{1}{r} \left(\Psi_r + \frac{\partial \Psi_\varphi}{\partial \varphi} \right) + \nu \frac{\partial \Psi_r}{\partial r} \right\}, \quad (5,6)$$

$$M_{r\varphi} = M_{\varphi r} = \frac{(1-\nu)D_b}{2} \left\{ \frac{\partial \Psi_\varphi}{\partial r} + \frac{1}{r} \left(\frac{\partial \Psi_r}{\partial \varphi} - \Psi_\varphi \right) \right\}, \quad (7)$$

$$Q_r = \kappa^2 Gh \left(\Psi_r + \frac{\partial w}{\partial r} \right), \quad Q_\varphi = \kappa^2 Gh \left(\Psi_\varphi + \frac{1}{r} \frac{\partial w}{\partial \varphi} \right), \quad (8,9)$$

where $D_b = Eh^3/12(1 - \nu^2)$ is the flexural rigidity, E is the modulus of elasticity, ν is the Poisson ratio, $\kappa^2 = \pi^2/12$ is the shear correction factor, and G is the shear modulus of the disk. Assume a harmonic variation with time,

$$\Psi_r(r, \varphi, t) = \psi_r(r, \varphi) \cos \omega t, \quad \Psi_\varphi(r, \varphi, t) = \psi_\varphi(r, \varphi) \cos \omega t, \quad w(r, \varphi, t) = W(r, \varphi) \cos \omega t, \quad (10)$$

to reduce Eqs. (2)–(4) to

$$\frac{\partial M_r}{\partial r} + \frac{1}{r} \frac{\partial M_\varphi}{\partial \varphi} + \frac{1}{r} (M_r + M_\varphi) - Q_r + \frac{\omega^2 \rho_d h^3}{12} \psi_r = 0, \quad (11)$$

$$\frac{\partial M_{r\varphi}}{\partial r} + \frac{1}{r} \frac{\partial M_\varphi}{\partial \varphi} + \frac{2}{r} M_{r\varphi} - Q_\varphi + \frac{\omega^2 \rho_d h^3}{12} \psi_\varphi = 0, \quad (12)$$

$$\frac{\partial Q_r}{\partial r} + \frac{1}{r} \frac{\partial Q_\varphi}{\partial \varphi} + \frac{1}{r} Q_r + \omega^2 \rho_d h W = 0. \quad (13)$$

The transverse deflection amplitude (W) and associated angular rotations (ψ_r and ψ_φ) are defined in terms of three potential functions ($\phi_1, \phi_2,$ and ϕ_3) as

$$\psi_r = (\sigma_1 - 1) \frac{\partial \phi_1}{\partial r} + (\sigma_2 - 1) \frac{\partial \phi_2}{\partial r} + \frac{1}{r} \frac{\partial \phi_3}{\partial \varphi}, \quad (14)$$

$$\psi_\varphi = \frac{(\sigma_1 - 1)}{r} \frac{\partial \phi_1}{\partial \varphi} + \frac{(\sigma_2 - 1)}{r} \frac{\partial \phi_2}{\partial \varphi} + \frac{\partial \phi_3}{\partial r}, \quad (15)$$

$$W = \phi_1 + \phi_2, \quad (16)$$

while introducing the following parameters:

$$\sigma_1, \sigma_2 = (\delta_2^2, \delta_1^2) \left(R\lambda^4 - \frac{1}{S} \right)^{-1}, \quad (17a-b)$$

$$\delta_2^2, \delta_1^2 = \frac{\lambda^4}{2} \left\{ R + S \pm [(R - S)^2 + 4\lambda^4]^{-1/2} \right\}, \quad (18a-b)$$

$$R = \frac{h^2}{12}, \quad S = \frac{D_b}{\kappa^2 Gh}, \quad \lambda^4 = \frac{\rho_d \omega^2 h}{D_b}. \quad (19a-c)$$

Substitution of Eqs. (3)–(9) and (14)–(16) in Eqs. (11)–(13) along with a series of subsequent manipulations yields

$$(\nabla^2 + \delta_1^2)\phi_1 = 0, \quad (\nabla^2 + \delta_2^2)\phi_2 = 0, \quad (\nabla^2 + \delta_3^2)\phi_3 = 0, \quad (20)$$

where ∇^2 is the harmonic differential operator, and another parameter is introduced as follows:

$$\delta_3^2 = 2\left(R\lambda^4 - \frac{1}{S}\right) / (1 - \nu). \quad (21)$$

The solutions to Eqs. (11)–(13) require the determination of the potential functions ϕ_1 , ϕ_2 , and ϕ_3 that must satisfy Eq. (20):

$$\phi_1(r, \varphi) = R_{n1} \sin(n\varphi), \quad \phi_2(r, \varphi) = R_{n2} \sin(n\varphi), \quad \phi_3(r, \varphi) = R_{n3} \cos(n\varphi). \quad (22a-c)$$

Introducing Eq. (22) into (20) yields:

$$r^2 \frac{d^2 R_{ni}}{dr^2} + r \frac{dR_{ni}}{dr} + (\delta_i^2 r^2 - n^2) = 0, \quad i = 1, 2, 3, \quad (23)$$

where n is typically a positive integer. The general solutions to Eqs. (23) involve ordinary and modified Bessel functions of the first and second kinds and the six constants of integration that are determined from the boundary conditions.

2.2. Thin plate theory

The thin plate theory essentially neglects the effects of rotary inertia and additional deflections caused by shear forces [5,6]. Consequently, the governing differential equation for transverse displacement $w(r, \varphi, t)$ in the mid-plane of the plate is

$$D_b \left(\frac{\partial^2}{\partial r^2} + \frac{1}{r} \frac{\partial}{\partial r} + \frac{1}{r^2} \frac{\partial^2}{\partial \varphi^2} \right)^2 w - \rho_d h \frac{\partial^2 w}{\partial t^2} = 0. \quad (24)$$

Solution to this equation is assumed as

$$w(r, \varphi, t) = W(r) \cos(n\varphi) e^{-i\omega t}. \quad (25)$$

Using Eqs. (24)–(25), the following Bessel’s equation is obtained:

$$\left(\frac{d^2}{dr^2} + \frac{1}{r} \frac{d}{dr} + \frac{n^2}{r^2} \right)^2 W - \lambda^4 W = 0. \quad (26)$$

General solution to this equation can be written as

$$W(r) = C_1 J_n(\lambda_{mn}r) + C_2 Y_n(\lambda_{mn}r) + C_3 I_n(\lambda_{mn}r) + C_4 K_n(\lambda_{mn}r), \quad (27)$$

where J_n and Y_n are the Bessel functions of first and second kinds and I_n and K_n are modified Bessel functions of first and second kinds. Here n is the order of the Bessel function representing the number of nodal diameters and m is the order of eigenvalues representing the number of nodal circles [2–5].

2.3. Eigensolutions for free–free boundaries

For the thick plate theory, free–free boundary conditions at the inner and outer radial edges can be expressed as follows:

$$\begin{aligned} M_r(a, \varphi) = M_{r\varphi}(a, \varphi) = Q_r(a, \varphi) = 0, \\ M_r(b, \varphi) = M_{r\varphi}(b, \varphi) = Q_r(b, \varphi) = 0. \end{aligned} \quad (28a-b)$$

From the expressions of M_r , $M_{r\varphi}$, and Q_r as defined in Eqs. (13)–(23) along with boundary conditions defined by Eq. (28), one could formulate the following equation in matrix form:

$$[T_{\text{THICK}}]\{C\} = \{0\}. \quad (29)$$

Here, $[T_{\text{THICK}}]$ is a 6×6 characteristic matrix with elements of various Bessel functions, C is an arbitrary coefficients vector and is the null vector. Refer to Ref. [8] for an analytical description of the elements of $[T_{\text{THICK}}]$. For the thin plate theory, boundary conditions of Eq. (28) are simplified as follows:

$$\begin{aligned} M_r(a, \varphi) = M_{r\varphi}(a, \varphi) = 0, \\ M_r(b, \varphi) = M_{r\varphi}(b, \varphi) = 0. \end{aligned} \quad (30a-b)$$

Given the relations between w and bending moments (M_r , $M_{r\varphi}$), the following equations can be derived for the boundaries satisfying Eq. (30):

$$\begin{aligned} \frac{\partial^2 w}{\partial r^2} + \nu \left(\frac{1}{r} \frac{\partial w}{\partial r} + \frac{1}{r^2} \frac{\partial^2 w}{\partial \varphi^2} \right) = 0, \\ \frac{\partial}{\partial r} \left(\frac{\partial^2 w}{\partial r^2} + \frac{1}{r} \frac{\partial w}{\partial r} + \frac{1}{r^2} \frac{\partial^2 w}{\partial \varphi^2} \right) + \frac{1-\nu}{r^2} \frac{\partial^2}{\partial \varphi^2} \left(\frac{\partial w}{\partial r} + \frac{w}{r} \right) = 0. \end{aligned} \quad (31a-b)$$

The characteristic matrix equation corresponding to thin plate theory, similar to Eq. (29), is

$$[T_{\text{THIN}}]\{C\} = \{0\}. \quad (32)$$

Here, $[T_{\text{THIN}}]$ is a 4×4 characteristic matrix and elements of this matrix are described in Refs. [5,6]. The characteristic or frequency equations are obtained from Eqs. (29) or (32).

2.4. Validation studies

Analytical solutions for the free–free boundaries, as obtained by both thin and thick plate theories, are compared in Table 3. Results of finite-element analyses and structural modal experiments are also provided for Disks I, II, and III. Only the first four modes are listed in Table 3 since the relevant upper frequency for acoustic radiation study for Disk I is 8 kHz. In the finite-element method (FEM), 11 out-of-plane modes have been obtained in the frequency range from 0 to 16 kHz with a model that includes 4,400 solid brick elements and 6,600 nodes [10]. In addition, mode shapes of Disk I from alternate analytical approaches are compared with numerical analysis in Fig. 2. As shown in this figure, the mode shapes from alternate plate theories are very similar in spite of differences in natural frequencies. In modal experiments, the excitation force $f(t)$ is applied in the z direction by an impulse hammer (PCB GK291C) at $\varphi = 0^\circ$ at the outer edge of the disk. The set up for structural modal experiment is explained in Fig. 3. The frequency range and

Table 3
Eigensolutions for Disks I, II and III with free–free boundaries

Disk	Mode indices		Non-dimensional eigenvalues $\lambda_{mn}^2 = \omega_{mn} a^2 (\rho_d h / D_b)^{1/2}$				ω_{mn} (kHz)
	<i>m</i>	<i>n</i>	Thick plate theory (Model A)	Thick plate theory (Model C)	Finite element (Model D)	Experiment (E)	
I $\beta=0.54$ $\bar{h}=0.21$	0	2	3.82	4.02	3.86	3.92	1.331
	1	0	8.85	9.80	8.69	9.02	3.063
	0	3	10.59	11.11	10.04	10.25	3.481
	1	1	15.42	17.55	13.57	14.00	4.756
II $\beta=0.59$ $\bar{h}=0.23$	0	2	3.62	3.90	3.72	3.72	1.500
	1	0	9.14	10.53	8.74	9.33	3.756
	0	3	10.04	10.73	9.75	9.78	3.938
	1	1	15.36	18.32	13.22	13.81	5.563
III $\beta=0.54$ $\bar{h}=0.11$	0	2	4.06	4.12	4.03	4.03	0.706
	1	0	9.55	9.82	8.99	9.53	1.669
	0	3	11.11	11.13	10.71	10.78	1.888
	1	1	16.86	17.59	15.27	15.99	2.800

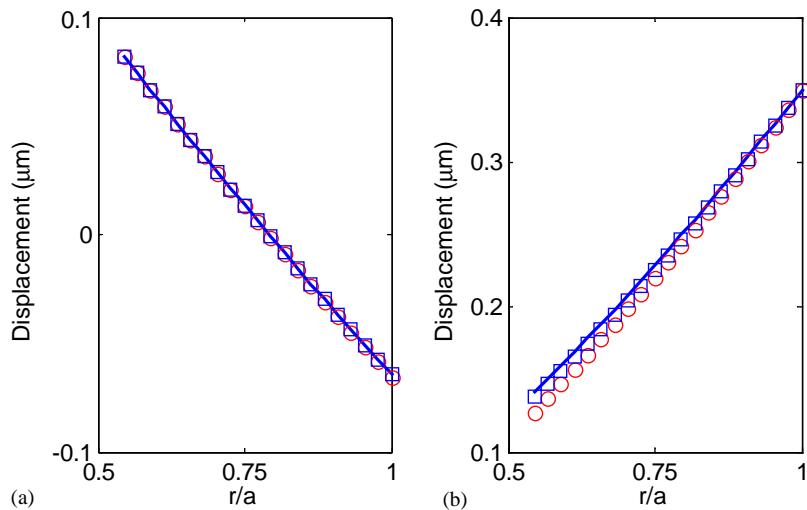


Fig. 2. Comparison of Disk I mode shapes given free–free boundaries. (a) (1,0) mode; (b) (0,2) mode. Key: □□□, thick plate theory (Model A); ○○○, thin plate theory (Model C); —, finite-element method (Model D).

resolution (Δf) of this experiment are set as 16 kHz and 1 Hz respectively. Natural frequencies (ω_{mn}) and modal damping ratios (ζ_{mn}) are extracted from accelerance spectra $\ddot{w}/f(\omega)$ where \ddot{w} is the acceleration and f is the applied force. As shown in Table 3, the finite-element predictions match well with measurements. Analytical solutions based on the thick plate theory produce more accurate answers than the ones that are based on the thin plate theory. Yet, even the thick plate

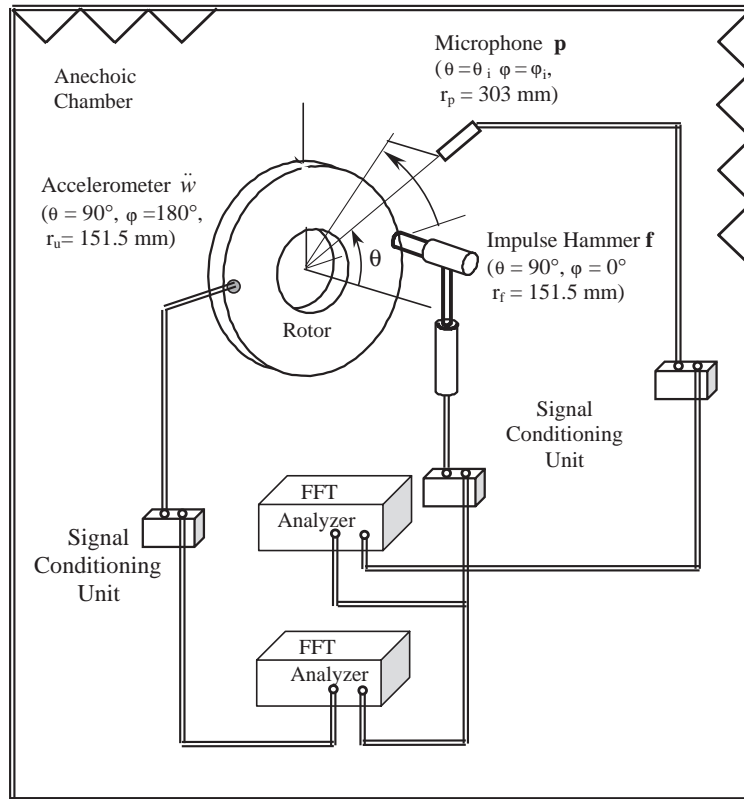


Fig. 3. Vibro-acoustic experiment used to measure structural $\ddot{w}/f(\omega)$ and acoustic $P/f(\omega)$ frequency response functions.

theory predictions show significant errors over the higher-frequency range. Also, it is obvious that differences between eigenvalues based on two alternate plate theories are proportional to the thickness ratio ($\bar{h} = h/a$).

Modal damping ratios are estimated from measured accelerance spectra using the half-power bandwidth method for every resonant peak and these results are summarized in Table 4. In addition, accelerance spectrum $\ddot{w}(r, \varphi)$ is calculated based on the numerical modal dataset using the forced vibration analysis in the FEM. These results are subsequently used as excitation to numerical or analytical methods for the calculation of far-field sound radiation. Fig. 4 compares computed and measured accelerance spectra and a good agreement over the given frequency range is observed. Dominant peaks in this figure correspond to the out-of-plane modes whose frequencies are listed in Table 3.

2.5. Effect of fixed-free boundaries

Eigensolutions for a disk with fixed-free boundaries can be easily calculated from the analytical solutions of Section 2.1. For the thick plate case, boundary conditions at $r = b$ (fixed) and $r = a$

Table 4
Measured modal damping ratios for Disk I

Mode Indices		Damping ratio (%)
<i>m</i>	<i>n</i>	
0	2	0.62
1	0	0.34
0	3	0.26
1	1	0.26

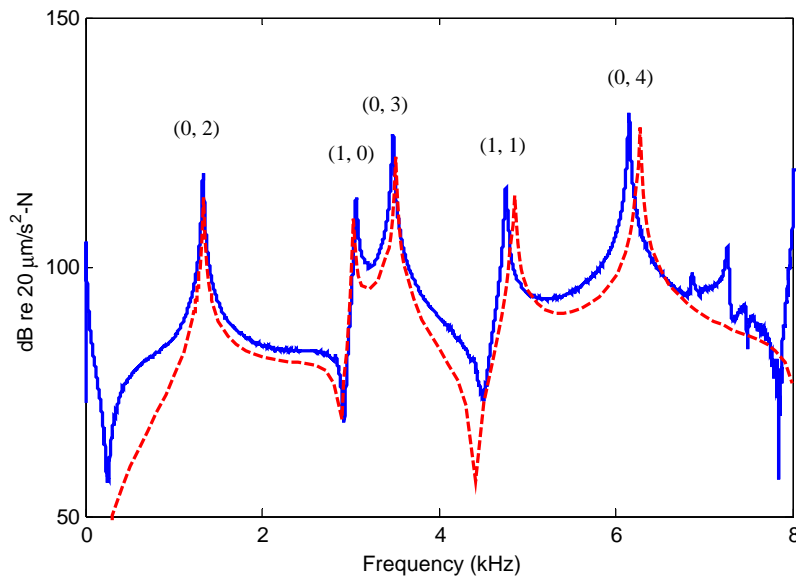


Fig. 4. Structural accelerances $\ddot{w}/f(\omega)$ at $r=151.5$ mm and $\varphi=180^\circ$ for Disk I with free–free boundaries. Key: ---, computed using FEM (Model D); —, measured (E).

(free) edges are expressed as

$$\begin{aligned} M_r(a, \varphi) = M_{r\varphi}(a, \varphi) = Q_r(a, \varphi) = 0, \\ W(b, \varphi) = \psi_r(b, \varphi) = \psi_\varphi(b, \varphi) = 0. \end{aligned} \tag{33a–b}$$

Likewise, for the thin plate case, these conditions are specified as

$$M_r(a, \varphi) = M_{r\varphi}(a, \varphi) = 0, \quad W_r(b, \varphi) = \frac{\partial W_r}{\partial r}(b, \varphi) = 0. \tag{34a–b}$$

From these boundary conditions, matrix equations similar to Eqs. (29) and (32) can be obtained and eigenvalues can be determined using the same procedure. In addition, natural frequencies are also calculated using the FEM and compared with alternate plate theories in Table 5. As in the free–free boundary case, eigensolutions based on the thick plate theory are much more accurate

Table 5
Eigensolutions of Disk I with fixed–free boundary conditions

Mode indices		Non-dimensional eigenvalue $\lambda_{mn}^2 = \omega_{mn} a^2 (\rho_d h / D_b)^{1/2}$			ω_{mn} (kHz)
m	n	Thick plate	Thin plate	FEM	FEM
0	0	11.96	15.72	13.61	4.623
0	1	13.43	16.05	13.63	4.628
0	2	15.28	17.52	14.28	4.849
0	3	18.75	21.17	16.81	5.709

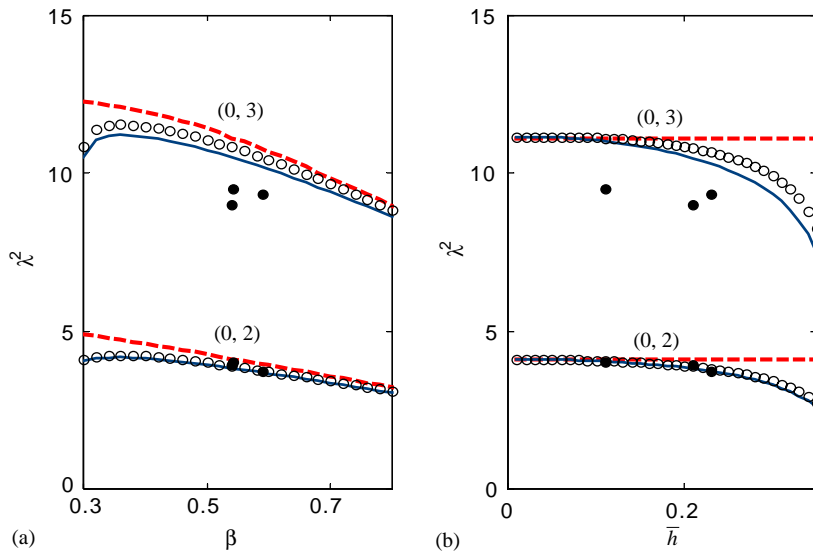


Fig. 5. Effect of geometry on the (0,2) and (0,3) modes of Disk I with free–free boundaries. (a) Effect of radii ratio (β); (b) effect of thickness ratio (\bar{h}). Key: —, thick plate theory (Model A); $\circ \circ \circ$, thick plate theory without rotary inertia effect (Model B); ---, thin plate theory (Model C); $\bullet \bullet \bullet$, measured (E).

than those given by the thin plate theory. Note that modal experiments are not attempted since it is difficult to experimentally simulate the perfect fixed boundary condition at $r = b$.

2.6. Effect of disk geometry on eigensolutions

As one can see from Eqs. (20)–(23), structural eigensolution of a thick annular disk are affected by the radii ratio ($\beta = b/a$), thickness ratio ($\bar{h} = h/a$), as well as by material properties. In this section, effects of β and \bar{h} on the non-dimensional eigenvalues are examined for selected modes of Disk I with free–free or fixed–free boundaries. In our investigation, such non-dimensional parameters are controlled by adjusting h and b for a fixed a . Eigenvalues are calculated using three alternate analytical methods based on models A, B, and C as described in Table 2. Results are shown in Figs. 5 and 6 where differences in the alternate formulations are evident. For the

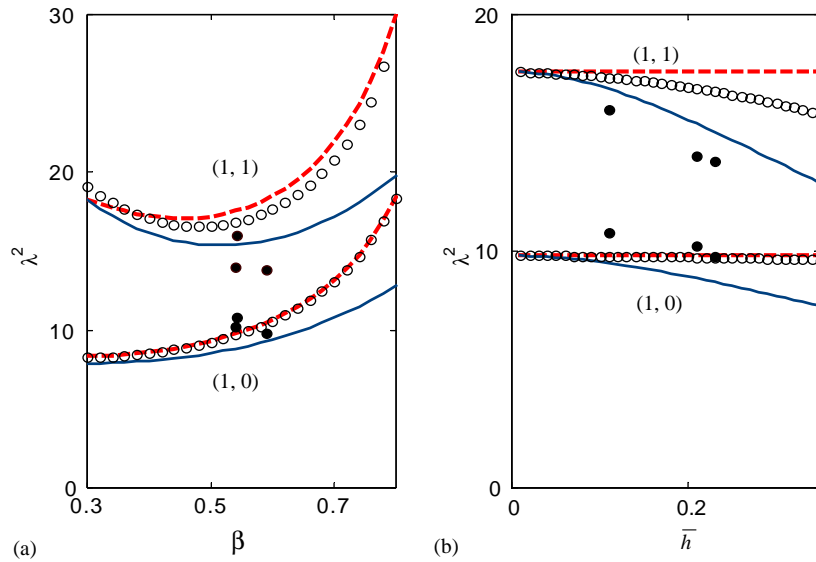


Fig. 6. Effect of geometry on the (1,0) and (1,1) modes of Disk I with free-free boundaries. (a) Effect of radii ratio (β); (b) effect of thickness ratio (\bar{h}). Key: —, thick plate theory (Model A); ○○○, thick plate theory without rotary inertia effect (Model B); ---, thin plate theory (Model C); ● ● ●, measured (E).

free-free disks, experimental and FEM results are also included in these figures for the sake of comparison. Differences between the λ_{mn}^2 values, based on alternate approaches, are proportional to \bar{h} for all modes. But as shown in Figs. 5(a) and 6(a), the effects of β are mode dependent. For example, differences are proportional to β for the (1,0) and (1,1) modes. Conversely, for the (0,2) and (0,3) modes, such differences are inversely proportional to β . The comparison of natural frequencies based on models A, B, and C suggests that differences between eigensolutions are mainly caused by the rotary inertia effect in the (1,0) and (1,1) modes and by the shear deformations in the (0,2) and (0,3) modes. Similar investigation has been executed for the fixed-free disk and results are given in Figs. 7 and 8. Differences between eigenvalues based on thick and thin plate theories appear to be caused by the shear deformations regardless of the mode type. Also, in this case, these differences are proportional to thickness and radii ratios for all modes.

3. Acoustic radiation calculations

3.1. Formulation

Sound radiation from the flexural vibrations of circular plates or annular disks has been examined by several investigators [11–15]. For instance, Thompson [11] computed self- and mutual radiation impedances of a uniformly vibrating annular or circular piston by integrating the far-field directivity function. Lee and Singh [12] proposed a polynomial approximation for

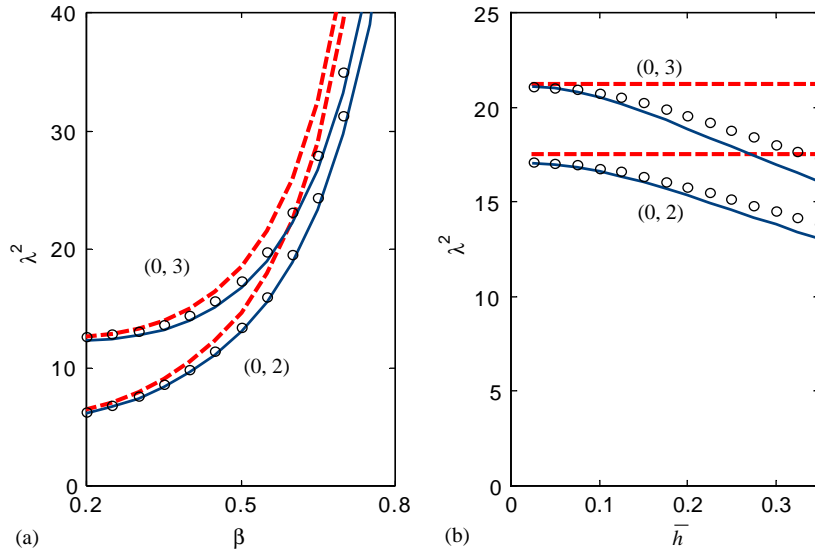


Fig. 7. Effect of geometry on the (0,2) and (0,3) modes of Disk I with fixed–free boundaries. (a) Effect of radii ratio (β); (b) effect of thickness ratio (\bar{h}). Key: —, thick plate theory (Model F); $\circ \circ \circ$, thick plate theory without rotary inertia effect (Model G); ---, thin plate theory (Model H).

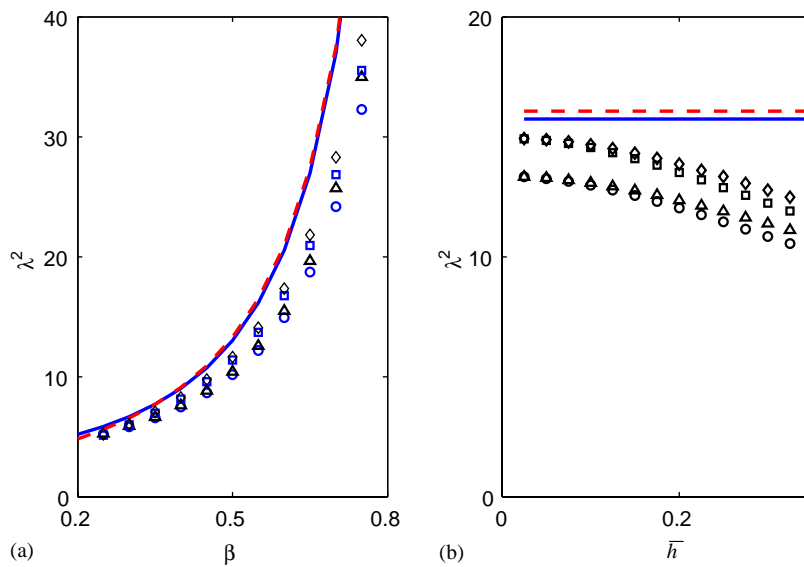


Fig. 8. Effect of geometry on the (1,0) and (1,1) modes of Disk I with fixed–free boundaries. (a) radii ratio (β); (b) thickness ratio (\bar{h}). Key: $\circ \circ \circ$, (0,0) mode with thick plate theory (Model F); $\triangle \triangle \triangle$, (0,0) mode with thick plate theory without rotary inertia effect (Model G); —, (0,0) mode with thin plate theory (Model H); $\square \square \square$, (0,1) mode with thick plate theory (Model F); $\diamond \diamond \diamond$, (0,1) mode with thick plate theory without rotary inertia effect (Model G); ---, (0,1) mode with thin plate theory (Model H).

modal acoustic power radiation from a thin annular disk using the far-field and radiation impedance approaches. Levine and Leppington [13] developed an analytical solution for active and reactive powers from a planar annular membrane given axisymmetric motions. Rdzanek and Engel [14] suggested asymptotic formulas for power from a thin annular disk with clamped edges. Wodtke and Lamancusa [15] investigated a circular plate using finite-element analysis and then calculated the radiation via the Rayleigh integral formula. However, none of these studies have examined radiation from a thick annular disk. Jungar and Feit [16] introduced simplified expressions of Helmholtz integral equation using short- and long-wavelength approximations. Finally, Fahline and Koopmann [17] used the same expressions for general radiators with sharp edges and obtained reliable results.

If acoustic scattering from the edges of a vibrating structure is neglected, sound radiation from that structure can be typically expressed in an integral form:

$$P(r_p) = \int_{S_s} \left(\frac{\partial g}{\partial \bar{n}}(r_p, r_s)p(r_p) - \frac{\partial p}{\partial \bar{n}}(r_s)g(r_p, r_s) \right) dS(r_s). \tag{35}$$

Here, P is the sound pressure amplitude, g is the free-field Green function, r_p and r_s are the position vectors of receiver and source positions and \bar{n} is the surface normal vector at r_s . For a non-planar source, the far- and free-field sound pressure can be expressed as Eq. (36) based on the plane-wave approximation within the short-wavelength limits [16] along with a reference to Fig. 9

$$P(r_p) = \frac{\rho_0 c_0 k}{4\pi} \int_{S_s} \frac{e^{ik|r_p-r_s|} \dot{W}(r_s)}{|r_p - r_s|} (1 + \cos \eta) dS. \tag{36}$$

Here, ρ_0 is the mass density of air, c_0 is the speed of sound, k is the acoustic wave number, and \dot{W} is the amplitude of vibratory velocity in the z direction at r_s . For an axially symmetric radiator such as a circular or annular plate, (m, n) th modal sound pressure from a normal plane can be expressed as follows by simplifying Eq. (36) using the Hankel transform [16]. Here, J_n is the Bessel function of order n , $R = |r_p|$ is the radius of the sphere on which the observation positions are defined, and θ and ϕ are the cone and azimuthal angles of the observation positions, respectively.

$$P_{mn}(R, \theta, \phi) = \frac{\rho_0 c_0 k e^{ik_m R_d}}{2R_d} \cos n\phi (-i)^{n+1} B_n[\dot{w}(r)](1 + \cos \eta), \tag{37a-d}$$

$$B_n[\dot{w}(r)] = \int_0^\infty \dot{w}(r) J_n(k_r r) r dr, \quad k_r = k \sin \theta; \quad R_d = |r_p - r_s|.$$

In our study, the observation positions are defined by a group of points having equal angular increments $(\Delta\varphi, \Delta\theta)$ on a sphere (S_V) that is centered at the disk center and sound pressures at all of the observation positions are calculated using Eqs. (36) or (37). The modal directivity function $D_{mn}(\theta, \phi)$ at frequency ω_{mn} can be defined from the modal pressure $P_{mn}(r_p)$ expression as follows:

$$D_{mn}(\theta, \phi) = RP_{mn}(R, \theta, \phi) e^{ik_{mn}R}. \tag{38}$$

From the far-field approximation, modal sound power Π_{mn} of the (m, n) th mode is calculated using the following equation:

$$\Pi_{mn} = \langle I_{mn} S_V \rangle_s = \frac{1}{2} \int_0^{2\pi} \int_0^\pi \frac{P_{mn}^2}{\rho_0 c_0} R^2 \sin \theta d\theta d\phi. \tag{39}$$

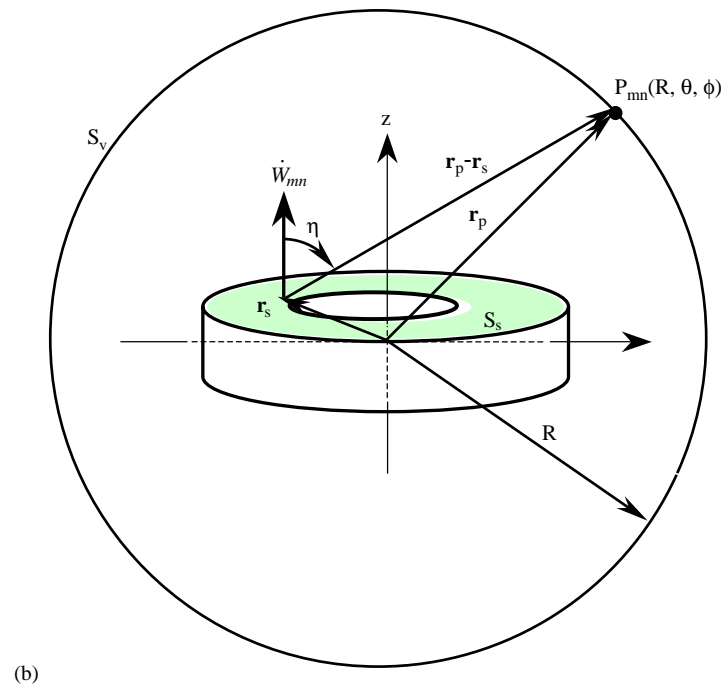
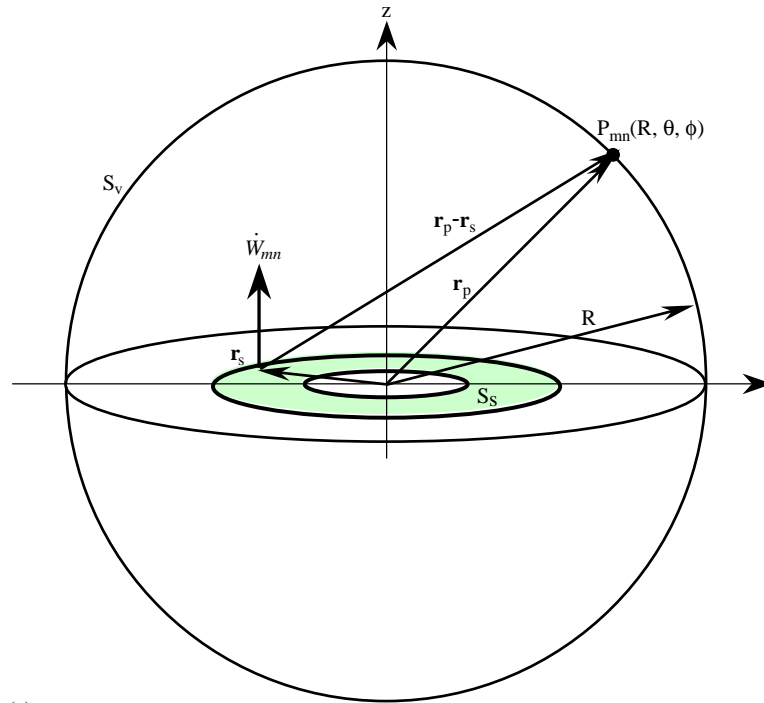


Fig. 9. Sound radiation from the out-of-plane vibration modes in the spherical coordinate system. (a) An unbaffled thin disk in full space; (b) an unbaffled thick disk in full space.

Here, I_{mn} is the acoustic intensity, and S_v is area of the control surface. The modal radiation efficiency σ_{mn} of an annular disk is determined from Π_{mn} as follows where $\langle |\dot{w}_{mn}|^2 \rangle_{t,s}$ is the spatially averaged mean-square velocity on the two normal surfaces of the annular disk:

$$\sigma_{mn} = \frac{\Pi_{mn}}{\langle |\dot{w}_{mn}|^2 \rangle_{t,s}}, \quad \langle |\dot{w}_{mn}|^2 \rangle_{t,s} = \frac{1}{2\pi(a^2 - b^2)} \int_b^a \int_0^{2\pi} \dot{W}^2 \, d\varphi \, dr. \quad (40a-b)$$

3.2. Thin plate approach

The classical method based on the thin plate theory does not consider the effect of h in sound radiation calculation. In this case, h is assumed to be negligible relative to other disk dimensions and sound radiation from the (m, n) th mode of a thick annular disk is generally calculated using the following equation by simultaneously considering sound radiation from two normal surfaces. In addition, R_d in Eq. (36) is approximated with R and Eq. (36) is simplified to yield the following expression for P_{mn} :

$$P_{mn}(R, \theta, \phi) = \frac{\rho_0 c_0 k_{mn} e^{ik_{mn}R}}{R} \cos n\phi (-i)^{n+1} B_n[\dot{w}(r)] \cos \theta. \quad (41)$$

As an alternative to Eq. (41), the results of structural analysis of Section 2 may be used. For example, define the approximate mode shape Ψ_{mn} and the corresponding modal surface velocity \dot{w}_{mn} as follows where polynomial functions are used to describe the flexural vibrations [12]:

$$\begin{aligned} \psi_{mn}(r, \varphi) &= \cos(n\varphi) \sum_{s=0}^N C_{mn,s}, \\ \dot{w}_{mn}(r, \varphi, t) &= \dot{W}(r, \varphi) e^{i\omega_{mn}t} = -\omega_{mn} C_{mn,s} r^s \cos(n\varphi) e^{i\omega_{mn}t}. \end{aligned} \quad (42a-b)$$

Here, $C_{mn,s}$ is an arbitrary constant. Substituting Eq. (42b) into Eq. (37), the far-field modal sound pressure P_{mn} is

$$P_{mn}(R, \theta, \phi) = \frac{\rho_0 c k_{mn} e^{ik_{mn}R_d}}{R_d} \cos n\phi (-i)^{n+1} \sum_{s=0}^N C_{mn,s} \int_b^a r^{s+1} J(k_{mn}r \sin \theta) \, dr \cos \theta. \quad (43)$$

By expanding the Bessel function of the first kind in terms of corresponding power series, the modal sound pressure can be expressed as

$$\begin{aligned} P_{mn}(R, \theta, \phi) &= \frac{\rho_0 c k_{mn} e^{ik_{mn}R_d}}{R_d} \cos n\phi (-i)^{n+1} \cos \theta \\ &\times \sum_{s=0}^N \sum_{l=0}^{\infty} \frac{C_{mn,s} (-1)^l (k_{mn} \sin \theta)^{2m+1} b^{n+s+2l+2}}{l!(n+l)! 2^{2l+n} (n+s+2l+2)} (1 - \beta^{n+s+2l+2}). \end{aligned} \quad (44)$$

The analytical method based on the thin plate theory (Model K) uses Eq. (44) for sound pressure calculations.

3.3. Thick plate approach

For the thick plate theory, we do not ignore the thickness (h) effect. Therefore, sound radiations from two normal surfaces should be simultaneously considered. With reference to Eq. (35) along with the far-field assumption, the angle η is approximated by θ for the normal surface facing the field point and by $-\theta$ on the opposite side. Consequently, the sound pressure at r_p is given by the sum:

$$P(r_p) = \frac{\rho_0 c k}{4\pi} \left(\int_{S_s} \frac{e^{ik|r_p-r_s|} \dot{W}(r_s)}{|r_p-r_s|} (1 + \cos \theta) + \int_{S_s} \frac{e^{ik|r_p-r'_s|} \dot{W}(r'_s)}{|r_p-r'_s|} (1 - \cos \theta) \right) dS. \quad (45)$$

Here, r'_s is the position vector of a source point on the normal surface that is away from the field point. In addition, $|r_p-r_s|$ and $|r_p-r'_s|$ are expressed as

$$\begin{aligned} R_d &= |r_p-r_s| = \sqrt{x^2 + y^2 + (z - \frac{h}{2})^2} \approx R \left(1 - \frac{hz}{R^2}\right) \approx R - \frac{h}{2} \cos \theta, \\ R'_d &= |r_p-r'_s| = \sqrt{x^2 + y^2 + (z + \frac{h}{2})^2} \approx R \left(1 + \frac{hz}{R^2}\right) \approx R + \frac{h}{2} \cos \theta, \\ R &= |r_p|, \quad x = R \sin \theta \cos \phi, \quad y = R \sin \theta \sin \phi, \quad z = R \cos \theta. \end{aligned} \quad (46a-f)$$

According to the far-field condition, R_d and R'_d in the denominator of Eq. (46) can be approximated by R , but the numerator terms cannot be replaced with R especially over the higher-frequency range. Substituting Eq. (46) into Eq. (45) and employing the Hankel transform used in Eq. (36), we find the following equations with a simplified R expression in the denominator.

$$\begin{aligned} P_{mn}^s(R, \theta, \phi) &= \frac{\rho_0 c k_{mn} e^{ik_{mn}R}}{2R} e^{-ik_{mn}\frac{h}{2}\cos \theta} \cos n\phi (-i)^{n+1} B_n[\dot{w}(r)], \\ P_{mn}^o(R, \theta, \phi) &= \frac{\rho_0 c k_{mn} e^{ik_{mn}R}}{2R} e^{ik_{mn}\frac{h}{2}\cos \theta} \cos n(\phi + \pi) (-i)^{n+1} B_n[\dot{w}(r)]. \end{aligned} \quad (47a-b)$$

As one can see from these equations, the disk thickness introduces a phase difference that is equal to $-k_{mn}(h/2)\cos \theta$ for the surface facing the field point and is $k_{mn}(h/2)\cos \theta$ for the surface away from the field point. The total far-field modal sound pressure is expressed by a sum of sound radiations from two normal surfaces

$$P_{mn}(R, \theta, \phi) = (1 + \cos \theta) P_{mn}^s(R, \theta, \phi) + (1 - \cos \theta) P_{mn}^o(R, \theta, \phi). \quad (48)$$

The semi-analytical (Model L) and analytical (Model J) methods based on the thick plate theory consider the effect of h and use Eq. (48) for the calculation of sound pressure.

4. Computational and experimental investigations of sound radiation

Modal acoustic radiation properties such as acoustic frequency response functions $P/f(\omega)$, modal acoustic power (Π_{mn}), and modal radiation efficiency (σ_{mn}) of Disk I are obtained using the analytical methods of Section 3. Furthermore, the same radiation properties are calculated with uncoupled, direct, exterior, and un baffled boundary element analyses [18]. In the computational

study (Model M), 6146 acoustic field points and 6144 elements are defined on the sphere (S_p) surrounding the disk that is represented by the finite-element model for structural dynamics. The center of this sphere coincides with the disk center. Excitations to this boundary element analysis (BEM) are the normal velocity distribution $\dot{W}(r, \varphi)$ on both normal surfaces that are obtained from the forced vibration analysis using the finite-element code (Model D). Analytical predictions and numerical analyses are verified by comparing results with measured data obtained from vibro-acoustic experiments conducted in an anechoic chamber as shown in Fig. 3. Far-field sound pressures are measured with a 6 mm microphone (MTS L130C10 combined with pre-amplifier MTS 130P10) at predetermined field points on a circle of $R = 303$ mm radius from the disk center in the plane of $\varphi = 0^\circ$ and $\theta = 90^\circ$. Considering the symmetries of the pressure distributions, P is measured in the range of $0^\circ \leq \theta \leq 90^\circ$ in the $\varphi = 0^\circ$ plane with an increment of $\Delta\theta = 2.5^\circ$ and over $0^\circ \leq \varphi \leq 90^\circ$ in the $\theta = 90^\circ$ plane with an increment of $\Delta\phi = 5^\circ$. The same radius (303 mm) is used in computational and analytical studies. Force and pressure signals are conditioned and analyzed via a 2-channel dynamic signal analyzer (HP 35670A) to obtain $p/f(\omega)$ spectra such as the one shown in Fig. 10.

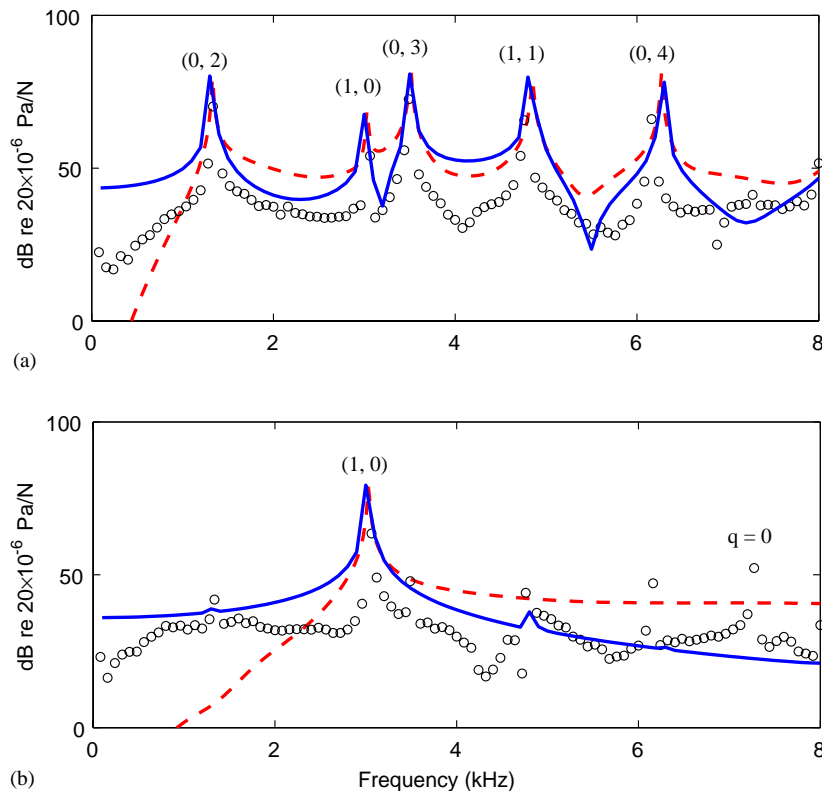


Fig. 10. Acoustic frequency response function $P/f(\omega)$ given unit impulsive force excitation $f(t)$ in the z direction at $r = 151.5$ mm. (a) $\theta = \pi/2$ and $\phi = 0$; (b) $\theta = 0$ and $\phi = 0$. Key: —, analytical calculation (Model L); ---, computed using BEM (Model M); $\circ \circ \circ$, measured. Here $q = 0$ is the radial mode.

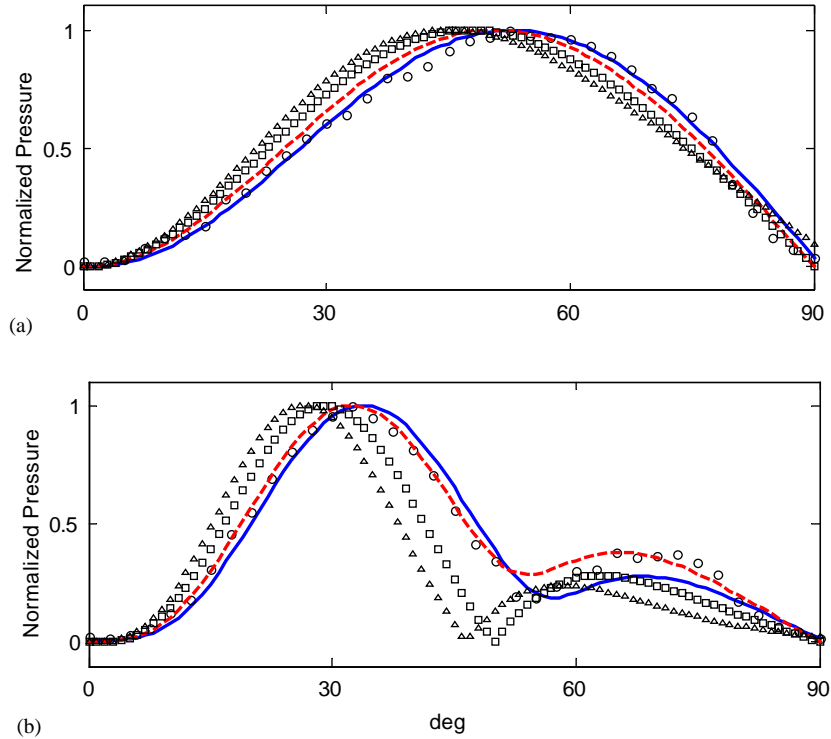


Fig. 11. Directivity pattern $D_{mn}(\theta)$ given $\phi=0$ and $R=303$ mm. (a) $m=0$, $n=2$ mode; (b) $m=0$, $n=3$ mode. Key: $\square\square\square$, analytical method based on thick plate theory (Model J); $\triangle\triangle\triangle$, analytical method based on thin plate theory (Model K); $---$, semi-analytical method (Model L); $---$, computed using BEM (Model M); $\circ\circ\circ$, measured.

The experimental directivity pattern $D(\theta, \phi)$ on the sphere S_V is synthesized from measured $P(\theta, \phi)$ data. Our analytical methods accurately predict the far-field sound pressure distributions. This is illustrated in Fig. 11 where $P(\theta, \phi)$ results from alternate analytical procedures are compared with measured and computed values for the (0,2) and (0,3) modes. Further, Table 6 compares directivity patterns in a pictorial form. Analytical predictions of Π_{mn} and σ_{mn} for two modes are compared with BEM code (Model C) and measured results in Table 7. In the experimental case, results at the discrete points over S_V have been synthesized using the measured $P_{mn}(\theta, \phi)$ data to yield Π_{mn} along with σ_{mn} . In this process, the measured $P_{mn}(\theta, \phi)$ profile is assumed to have a perfect sinusoidal variation in the ϕ direction. As shown in Tables 6 and 7, acoustic radiation properties obtained using analytical solutions (Models J, K, and L) match well with computational predictions (Model M) and measurements.

5. Effect of key parameters on modal radiation

As shown in Section 3, natural frequencies and modes of a thick annular disk are affected by its geometry and boundaries. Furthermore, Eqs. (44)–(45) illustrate that P_{mn} depends on disk geometry, vibrating mode and frequency. In this section, effects of the radii ratio ($\beta=b/a$),

Table 6
Comparison of directivity patterns for selected modes of Disk I

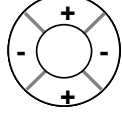
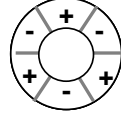
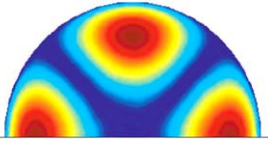
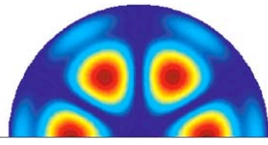
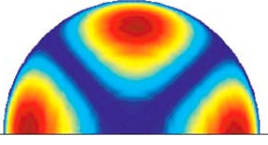
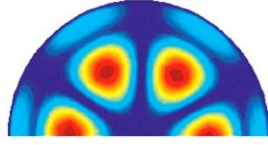
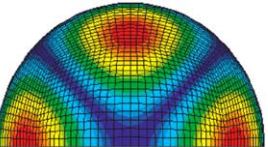
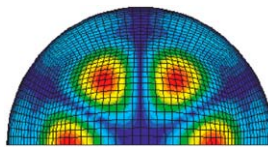
Structural mode	(0, 2) Mode	(0, 3) Mode
		
Analytical method		
Measured		
Computed using BEM		

Table 7
Comparison of modal acoustic power and radiation efficiency levels for selected out-of-plane modes of Disk I

Mode (m, n)	Measured	BEM (Model O)	Semi-analytical (Model L)	Analytical	
				Thick plate (Model J)	Thin plate (Model K)
Π_{mn} , (dB re 1 pW)					
(1,1)	70.1	70.7	71.6	70.1	70.9
(0,3)	75.3	76.3	76.2	75.1	74.8
σ_{mn}					
(1,1)	0.77	0.75	1.08	1.23	1.06
(0,3)	0.81	1.01	1.01	1.28	1.14

thickness ratio ($\bar{h} = h/a$), and boundary conditions on modal sound radiation are studied through variations in $\langle |\dot{w}_{mn}|^2 \rangle_{t,s}$, Π_{mn} and σ_{mn} as introduced by changes in key parameters. As a first step, natural frequencies and mode shapes corresponding to a specific geometric configuration are calculated using thin or thick plate theory and then the modal surface velocities are defined from the corresponding structural eigensolutions. Then, the modal far-field sound pressures are calculated using Eq. (43) or (45). Finally, Π_{mn} and σ_{mn} are obtained from the sound pressure data using Eqs. (39)–(40). In this particular study, the amplitudes of modal vibrations are intentionally adjusted to get the same modal velocity amplitudes regardless of variations in the natural frequencies for a given geometric configuration.

5.1. Effects of radii ratio

First, the effect of β is investigated using Disk I. The results of this investigation are summarized in Figs. 12 and 13, where $\langle |\dot{w}_{mn}|^2 \rangle_{t,s}$ and σ_{mn} are significantly affected by β . For a limiting case of $\beta \rightarrow 0$ when the annular disk turns into a circular disk, sound radiation can be solved using the same solution. And, for the other limiting case when $\beta \rightarrow 1$, the annular disk can be considered as a thin cylinder that cannot generate sound with its out-of-plane vibration. As shown in Fig. 12, $\langle |\dot{w}_{mn}|^2 \rangle_{t,s}$ and σ_{mn} for (0,2) and (0,3) modes converge to 0 as $\beta \rightarrow 1$ irrespective of plate theories. But, as shown in Fig. 13, σ_{mn} values for (1,0) and (1,1) modes based on thin plate theory significantly fluctuate with β even in the case of $\beta \rightarrow 1$ though the corresponding $\langle |\dot{w}_{mn}|^2 \rangle_{t,s}$ values monotonically decrease. Conversely, σ_{mn} values for (1,0) and (1,1) modes based on the thick plate theory do not show much fluctuation with β . It is conceivable that Π_{mn} values based on

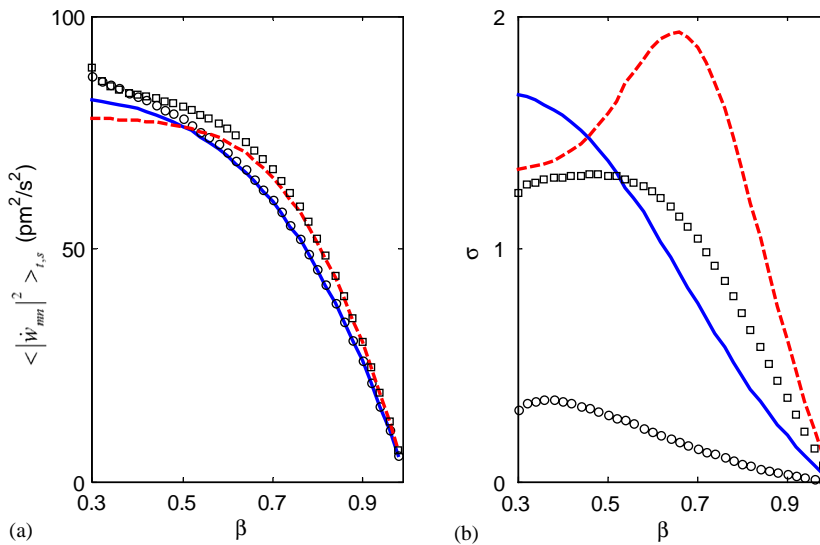


Fig. 12. Effect of radii ratio on the modal sound radiation based on alternate plate theories. (a) Spatially averaged mean-square velocity $\langle |\dot{w}|^2 \rangle_{t,s}$; (b) radiation efficiency σ . Key: $\circ \circ \circ$, (0,2) mode with thick plate theory (Model J); —, (0,2) mode with thin plate theory (Model K); $\square \square \square$, (0,3) mode with thick plate theory (Model J); ---, (0,3) mode with thin plate theory (Model K).

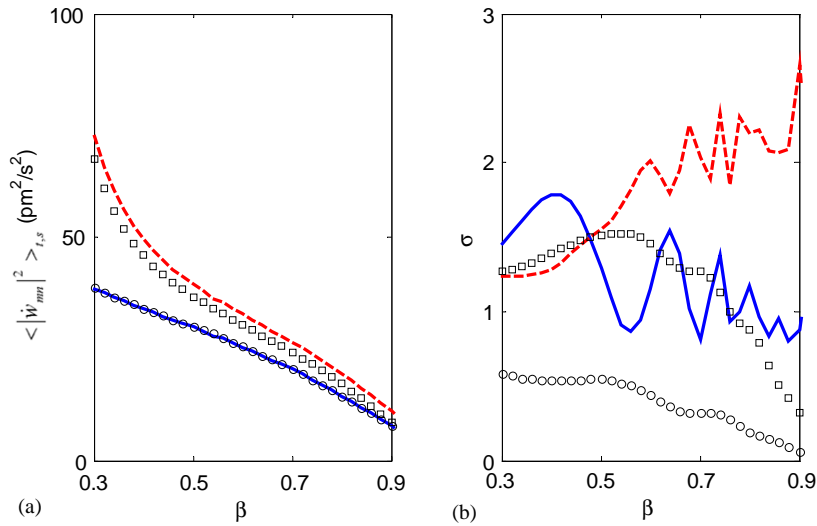


Fig. 13. Effect of radii ratio on the modal sound radiation based on alternate plate theories. (a) Spatially averaged mean-square velocity; (b) radiation efficiency σ . Key: $\circ \circ \circ$, (1,0) mode with thick plate theory (Model J); —, (1,0) mode with thin plate theory (Model K); $\square \square \square$, (1,1) mode with thick plate theory (Model J); ---, (1,1) mode with thin plate theory (Model K).

the thin plate theory fluctuate with β but the same values based on the thick plate theory are stable.

5.2. Effects of thickness

Next, \bar{h} is selected as an independent variable and it is varied from 0.025 to 0.35 with a nominal value of $\bar{h}_0 = 0.21$. Results are summarized in Figs. 14 and 15 where one can observe considerable variations in σ_{mn} . The $\langle |\dot{w}_{mn}|^2 \rangle_{t,s}$ values based on the thin plate theory are constant irrespective of the mode type. Conversely, the same data based on the thick plate theory are mode dependent. For instance, $\langle |\dot{w}_{mn}|^2 \rangle_{t,s}$ is proportional to \bar{h} for (0,2), (0,3) or (1,0) modes, but is inversely proportional to \bar{h} for (1,1) mode. As shown in Section 2, natural frequencies of the out-of-plane modes are proportional to h . If the disk thickness is small enough such that the natural frequency for a specific mode is below the critical frequency, the modal sound radiation is very low [16]. For this reason, σ_{mn} values are very low in the region of small \bar{h} regardless of the mode type as shown in Figs. 14 and 15. Furthermore, for the thick plate theory, phase difference between sound pressures radiated from two normal surfaces is proportional to \bar{h} and the effect of this phase difference should be considered in addition to the effect of natural frequency change. For the thin plate theory that considers sound pressure from only one normal surface, radiation is affected only by the natural frequency variation.

5.3. Effects of boundary conditions

The effect of fixed–free boundary conditions on sound radiation is finally studied. Typical Π_{mn} and σ_{mn} of two out-of-plane modes for Disk I with either free–free or fixed–free boundary

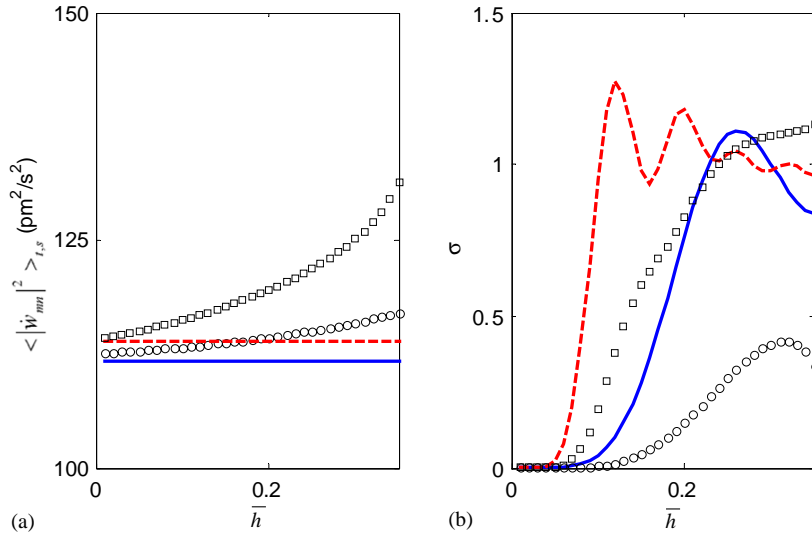


Fig. 14. Effect of thickness ratio on the modal sound radiation based on alternate plate theories. (a) Spatially averaged mean-square velocity $\langle |\dot{w}|^2 \rangle_{t,s}$; (b) radiation efficiency σ . Key: $\circ \circ \circ$, (0,2) mode thick with plate theory (Model J); —, (0,2) mode with thin plate theory (Model K); $\square \square \square$, (0,3) mode with thick plate theory (Model J); ---, (0,3) mode with thin plate theory (Model K).

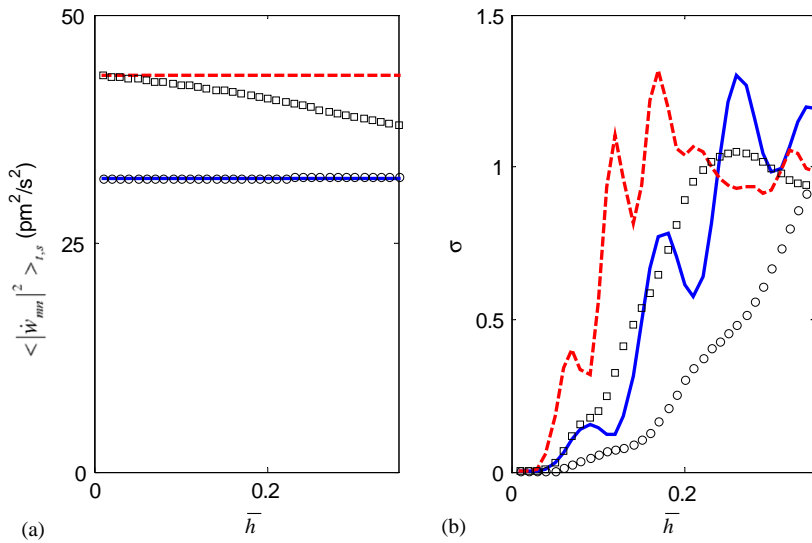


Fig. 15. Effect of thickness ratio on the modal sound radiation based on alternate plate theories. (a) Spatially averaged mean-square velocity $\langle |\dot{w}|^2 \rangle_{t,s}$; (b) radiation efficiency σ . Key: $\circ \circ \circ$, (1,0) mode with thick plate theory (Model J); —, (1,0) mode with thin plate theory (Model K); $\square \square \square$, (1,1) mode with thick plate theory (Model J); ---, (1,1) mode with thin plate theory (Model K).

conditions are listed in Table 8. The modal acoustic powers and radiation efficiencies for modes with the same number of nodal diameters (n) significantly change when the inner edge is clamped. For example, Π_{02} and σ_{02} increase with fixed–free boundaries due to the increases in the corresponding natural frequencies. For instance, ω_{02} goes up from 1.31 kHz (below the critical frequency that is around 2.0 kHz) to 4.85 kHz (above the critical frequency). Also, Π_{mn} and σ_{mn} for $n=0$ and $n=1$ modes, significantly increase due to the elimination of a nodal circle in the corresponding mode shapes. In addition, directivity patterns of two sample modes with fixed–free boundaries are numerically calculated and compared in Fig. 16 with those with free–free boundaries

Table 8
Modal acoustic powers and radiation efficiencies for first four out-of-plane modes with fixed–free or free–free boundaries

Boundaries	Mode indices	ω_{mn} (kHz)	Π_{mn} (dB re 1 pW)	σ_{mn}
Free–free	(0,2)	1.31	70.9	0.263
	(1,0)	2.95	67.2	0.379
	(0,3)	3.41	76.3	1.030
	(1,1)	4.61	70.7	0.808
Fixed–free	(0,0)	4.62	69.7	0.900
	(0,1)	4.63	73.4	0.884
	(0,2)	4.85	73.2	0.878
	(0,3)	5.71	73.7	0.883

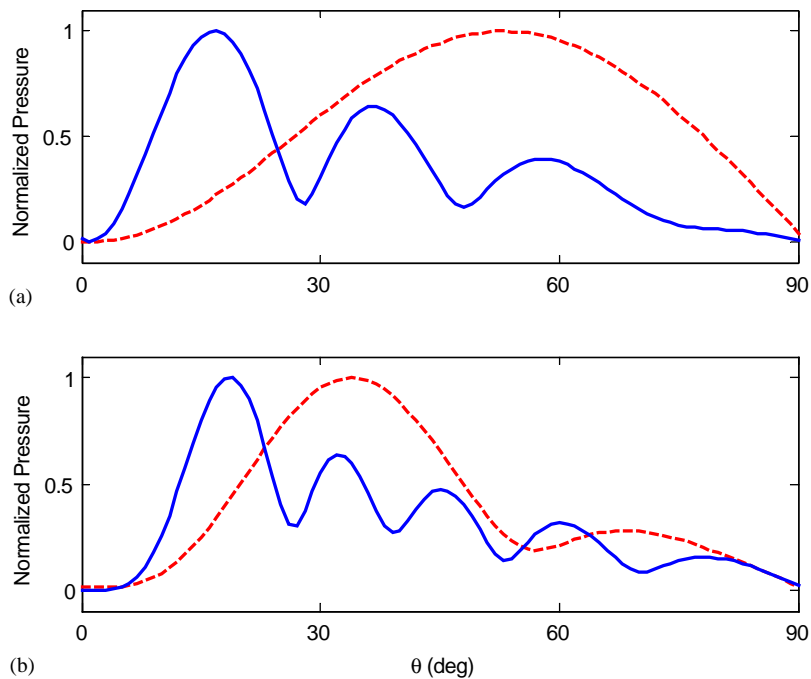


Fig. 16. Modal directivity patterns of Disk I with alternate boundary conditions. (a) $n=2$ modes; (b) $n=0$ modes. Key: —, fixed–free; ---, free–free boundary condition.

boundaries. The application of fixed–free boundary conditions increases the number of ripples in the θ direction for both modes.

6. Conclusion

This article has proposed a new analytical solution that explicitly considers the disk thickness effect on sound radiation from out-of-plane modes. In addition, our semi-analytical procedure combines the computationally obtained disk surface velocities with analytical solutions for sound radiation. A comparative evaluation of thin and thick plate theories shows that the thick plate theory is more accurate when predictions are compared with computational codes (such as FEM and BEM) and vibro-acoustic experiments. Our procedure can be efficiently used to conduct parametric studies such as the ones reported in this article by varying the radii or thickness ratio. In particular, one can easily analyze the limiting cases of a circular plate and a thin cylinder considering only the out-of-plane flexural modes. In a future article, we will simultaneously consider both out-of-plane and in-plane components of the disk vibration. Modal interaction effects and sound radiation from coupled modes will also be studied.

Acknowledgment

This project has been supported by the Center for Automotive Research Industrial Consortium and the sponsors include Bosch, CRF Fiat, Delphi Chassis, Dow Automotive, Ford, Edison Welding Institute, General Motors and LuK over the 1999–2001 period.

References

- [1] A.W. Leissa, *Vibration of Plates*, NASA SP-160 1969.
- [2] A.W. Leissa, Recent Research and plate vibration, 1981–1985—part 1: classical theory, *The Shock and Vibration Digest* 19 (3) (1987) 10–24.
- [3] A.W. Leissa, Recent research and plate vibration, 1981–1985—part 2: complicating effects, *The Shock and Vibration Digest* 19 (3) (1987) 10–24.
- [4] A.W. Leissa, *Vibrations of Plates*, Acoustical Society of America, New York, 1993.
- [5] S.M. Vogel, D.W. Skinner, Natural frequencies of transversely vibrating uniform annular disk, *Journal of Applied Mechanics* December 32 (1965) 926–931.
- [6] T.B. Gabrielson, Frequency constants for transverse vibration of annular disks, *Journal of the Acoustical Society of America* 105 (6) (1999) 3311–3317.
- [7] R.D. Mindlin, H. Deresiewicz, Thickness-shear and flexural vibration of a circular disk, *Journal of Applied Physics* 25 (10) (1954) 1329–1332.
- [8] O.G. Mcgee, C.S. Huang, A.W. Leissa, Comprehensive exact solutions for free vibrations of thick annular sectorial plates with simply supported radial edges, *International Journal of Mechanical Science* 37 (5) (1995) 537–566.
- [9] C.M. Wang, V. Thevendran, Vibration analysis of annular plates with concentric support using a variant of Rayleigh–Ritz method, *Journal of Sound and Vibration* 163 (1) (1993) 137–149.
- [10] *I-DEAS User's Manual*, version 8.2, SDRC, USA, 2000.

- [11] W. Thompson Jr., The computation of self- and mutual-radiation impedances for annular and elliptical pistons using Bouwkamp integral, *Journal of Sound and Vibration* 17 (2) (1971) 221–233.
- [12] M.R. Lee, R. Singh, Analytical formulations for annular disk sound radiation using structural modes, *Journal of the Acoustical Society of America* 95 (6) (1994) 3311–3323.
- [13] H. Levine, F.G. Leppington, A note on the acoustic power output of a circular plate, *Journal of Sound and Vibration* 121 (5) (1988) 269–275.
- [14] W.P. Rdzanek Jr., Z. Engel, Asymptotic formula for the acoustic power output of a clamped annular plate, *Applied Acoustics* 60 (5) (2000) 29–43.
- [15] H.W. Wodtke, J.S. Lamancusa, Sound power minimization of circular plates through damping layer placement, *Journal of Sound and Vibration* 215 (5) (1998) 1145–1163.
- [16] M.C. Junger, D. Feit, *Sound, Structures, and their Interactions*, MIT Press, New York, 1985.
- [17] J.B. Fahline, G.H. Koopmann, Numerical implementation of the lumped parameter model for the acoustic power of a vibrating structure, *Journal of the Acoustical Society of America* 102 (1) (1996) 179–192.
- [18] *SYSNOISE User's manual*, version 5.4, NIT, Belgium, 1999.